Multiple population-period transient spectroscopy (MUPPETS) in excitonic systems

Haorui Wu and Mark A. Berg

Citation: J. Chem. Phys. **138**, 034201 (2013); doi: 10.1063/1.4773982
View online: http://dx.doi.org/10.1063/1.4773982
View Table of Contents: http://jcp.aip.org/resource/1/JCPSA6/v138/i3
Published by the American Institute of Physics.

Multiple population-period transient spectroscopy (MUPPETS) in excitonic systems

Haorui Wu and Mark A. Berg[a)]
Department of Chemistry and Biochemistry, University of South Carolina, Columbia, South Carolina 29208, USA

(Received 2 October 2012; accepted 11 December 2012; published online 15 January 2013)

Time-resolved experiments with more than one period of incoherent time evolution are becoming increasingly accessible. When applied to a two-level system, these experiments separate homogeneous and heterogeneous contributions to kinetic dispersion, i.e., to nonexponential relaxation. Here, the theory of two-dimensional (2D) multiple population-period transient spectroscopy (MUPPETS) is extended to multilevel, excitonic systems. A nonorthogonal basis set is introduced to simplify pathway calculations in multilevel systems. Because the exciton and biexciton signals have different signs, 2D MUPPETS cleanly separates the exciton and biexciton decays. In addition to separating homogeneous and heterogeneous dispersion of the exciton, correlations between the exciton and biexciton decays are measurable. Such correlations indicate shared features in the two relaxation mechanisms. Examples are calculated as both 2D time decays and as 2D rate spectra. The effect of solvent heating (i.e., thermal gratings) is also calculated in multidimensional experiments on multilevel systems. © *2013 American Institute of Physics*. [http://dx.doi.org/10.1063/1.4773982]

I. INTRODUCTION

Kinetic measurements are a major subset of physical chemistry and take on many different forms appropriate to different processes and timescales. Nonetheless, almost all are one dimensional (1D): a single period of time exists between a single perturbation of the system and a later detection of its evolved state. Our group has been exploring multidimensional kinetics in which there is more than one perturbation, and thus, more than one period of time evolution.[1–10] We have called our approach, which uses weak optical perturbations, multiple population-period transient spectroscopy (MUPPETS). So far, its focus has been on nonexponential relaxation (rate dispersion) in two-level systems. In those systems, MUPPETS can separate homogeneous and heterogeneous contributions to rate dispersion. This paper lays a theoretical foundation for MUPPETS in multilevel systems and especially in excitonic systems—those with equally spaced levels and optical transitions and relaxations that occur in single steps. The most important new features are the ability to accurately separate exciton and biexciton dynamics and to measure correlations in the rate dispersion of exciton and biexciton relaxation. Related experimental results on exciton and biexciton dynamics in CdSe nanoparticles will be published in the near future.[11,12]

The concept of MUPPETS is illustrated in Fig. 1. A total of six pulses are used: three (1–3) simultaneous pairs (*a* and *b*) separated by two times, τ_1 and τ_2. Each pair causes an incoherent transition, i.e., a transition from one quantum mechanical population to another. Any coherence is assumed to be quenched by rapid dephasing. The novel aspect of MUPPETS is that the correlated relaxation of the population during two time periods is measured. Neither ensemble averaging nor relaxation of the molecule occurs between these periods, so different processes are accessible than in experiments with only one relaxation time. Understanding the resulting multidimensional correlation functions when several population states are accessible is a primary aim of this paper.

The pulses in each pair come from different directions, so the populations consist of spatial gratings.[13–15] Detection is by diffraction of pulse 3*a* from the final population grating and heterodyning the diffracted light with pulse 3*b*. (Practical detection schemes also account for diffraction in the opposite direction.[4]) As Fig. 1(a) suggests, it is possible to arrange the phase-matching geometry such that diffraction only occurs from planes created by the combined action of all four excitation pulses. These more technical aspects of the experiment will not be treated here. It is only important to know that it is practical to isolate a signal that is confined to exactly one electric-field interaction with each of the six pulses.

As with 1D kinetics, theoretical concepts transcend the various experimental implementations needed for different timescales and processes. In existing experiments, MUPPETS has focused on electronic-state relaxation on subnanosecond timescales. However, the theoretical ideas developed here are equally applicable to any timescale. With modest modification, they can also find application to other types of perturbation and other relaxation processes.

MUPPETS has strong parallels to multidimensional coherence spectroscopy (MDCS). MUPPETS measures multiple periods of incoherent evolution (kinetic rates), whereas MDCS measures multiple periods of coherent evolution (spectral frequencies). MDCS began with two-level systems, in which they give "echo" phenomena.[16,17] These experiments separate homogeneous and inhomogeneous contributions to spectral linewidths, just as MUPPETS of two-

a)Author to whom correspondence should be addressed. Electronic mail: berg@sc.edu.

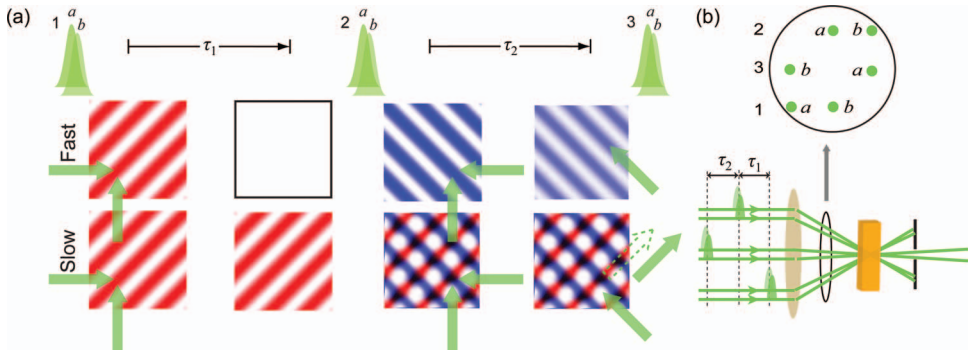

FIG. 1. Schematic of the MUPPETS experiment. (a) The upper and lower panels represent rapidly and slowly relaxing subensembles within the sample. Two simultaneous pulses (1*a* and 1*b*) from different directions intersect in the sample to create a spatial grating of excited-state molecules (red). After a time τ_1, a second pair of pulses (2*a* and 2*b*) create a second grating of excited molecules (blue). The slow subensemble now contains vertical diffraction planes formed by regions that have interacted twice (black), once (red and blue) and never (white). After an additional time τ_2, pulse 3*a* is diffracted from these planes and is combined with pulse 3*b* for heterodyne detection. The diffraction isolates the signal unique to one interaction with the first excitation and one interaction with the second excitation. (b) An accurate representation of the pulse directions used in the experiment: tan – lens, orange – sample.

level systems separates homogeneous and heterogeneous rate dispersion. When MDCS was extended to multilevel systems, it became various forms of spectral correlation spectroscopy, which reveal coupling between different spectral transitions.[18–22] MDCS is well established in nuclear magnetic resonance[18,19] and, more recently, has been extended to electronic[20] and vibrational[21,22] transitions. In the latter two forms, it has been especially valuable in excitonic systems,[23–29] where the transitions are strongly overlapped in 1D spectra. By analogy, one anticipates that MUPPETS in multilevel systems will probe correlations in the relaxation of different transitions and will be especially relevant in excitonic systems, where spectral discrimination of different transitions can be difficult.

One goal of the paper is to clarify the meaning of the intertransition correlations that we anticipate. Another is to illustrate the interplay of the intertransition and intratransition contributions to the total experimental signal. To tackle these problems, we first develop simplified methods for calculating multidimensional incoherent signals in excitonic systems and then use them to calculate results for several simple, limiting models.

In two-level systems, it is common to reduce the dimensionality of the problem by changing the basis set. The total population is invariant, and only the dynamics of the population difference need to be calculated. The primary simplifications in the current calculations come from extending this idea to multilevel systems. A nonorthogonal coordinate system is required, but this feature is easily handled by the Hilbert-space formalism that we introduced previously.[5,6] The primary new difficulty in multilevel systems is the possibility of cross-relaxation between basis states. Fortunately, this effect is minimized when higher excitons relax faster than lower excitons. This situation is common due to processes that are called exciton–exciton annihilation in molecular systems or Auger relaxation in semiconductors. Approximations for this case are found. Section II develops the general formalism, and then Sec. III looks in more detail at two-dimensional (2D) MUPPETS for several different energy-level schemes.

These results lead to several useful results that are explored in Sec. IV. Separating exciton and biexciton kinetics can be difficult when the spectral exciton shift is small. MUPPETS is a sensitive and robust method for separating exciton and biexciton dynamics that does not rely on spectral separation. It is also insensitive to the formation of photoproducts, which can complicate power-dependent measurements. In general, the level of coupling between zero-order chromophores needed to create an exciton for purposes of MUPPETS (an incoherent exciton) is much lower than that needed to create an exciton for purposes of coherent spectroscopy (a coherent exciton). Thus, MUPPETS can be useful for studying weakly coupled systems.

Example calculations are presented on four model systems with identical 1D kinetics in Sec. IV C. These models mix homogeneous and heterogeneous exciton relaxation with biexcitons that are either correlated or uncorrelated with the exciton relaxation. Despite having identical 1D kinetics and despite the overlap of intra- and intertransition features, each model produces very different 2D results and would be readily distinguishable in a 2D MUPPETS experiment. Rate correlation between different transitions is shown to be analogous to homogeneous kinetics on a single transition. Correlation between exciton and biexciton relaxation is possible whether or not the individual transitions are homogeneous or heterogeneous. Intertransition rate correlations indicate a shared feature in the two relaxation mechanisms such as dependence on a common bath mode.

Real MUPPETS experiments detect not only the resonant signal due to the chromophore, but also see solvent heating due to chromophore relaxation.[7] These thermal effects are the multidimensional extension of thermal-grating spectroscopy.[13–15] They are both a complication to measuring the resonant signal and a potential route to measuring nonradiative relaxation between spectroscopically dark states. The theory needed to calculate thermal effects in multilevel MUPPETS experiments is developed in Sec. V.

II. THEORY FOR MULTISTATE SYSTEMS

The Hilbert-space pathway formalism for calculating multidimensional incoherent experiments has been discussed in detail previously.[5,6,10] In this formalism, as the number

of states in the system increases, the number of pathways increases combinatorially. This section seeks to simplify such calculations. Section II A summarizes previous Hilbert-space results in a convenient notation. Section II B introduces a new basis set to simplify these calculations in a general multistate system. Section II C then specializes to excitonic systems, which will be the focus of the remainder of the paper.

A. Review of incoherent Hilbert-space calculations

The signal from an N-dimensional heterodyned experiment is the change in fluence of the $(N+1)$th (local oscillator) beam $\delta I_{N+1}(\Phi)$ relative to its total fluence I_{N+1}, as a function of the local-oscillator–probe phase difference Φ. This change can be expressed as an absorbance $A^{(N)}(\Phi; \tau_N, \ldots, \tau_1)$,

$$A^{(N)}(\Phi; \tau_N, \ldots, \tau_1) = (-1)^N \frac{\delta I_{N+1}(\Phi)}{I_{N+1}}, \tag{1}$$

where τ_n is the time interval between pulses n and $n+1$. Fourier transforming the phase-dependence extracts a complex absorbance $A^{(N)}(\tau_N, \ldots, \tau_1)$, which obeys a generalized Beer's law,[7,10]

$$A^{(N)}(\tau_N, \ldots, \tau_1) = (-1)^N \rho L \langle \boldsymbol{\sigma}_D \rangle^\circ. \tag{2}$$

This expression contains the detection cross-section operator $\boldsymbol{\sigma}_D$, the number density of solute molecules ρ, and the length of the sample L.

The expectation value of $\boldsymbol{\sigma}_D$ is calculated as a matrix element in the incoherent Hilbert space,

$$\langle \boldsymbol{\sigma}_D \rangle^\circ = [I|\boldsymbol{\sigma}_D|f(\tau_N, \ldots, \tau_1)]^\circ, \tag{3}$$

where $[I|$ is the identity state [see Eq. (17)] and $|f]$ is the final state of the system at the time of detection. The degree sign indicates that the calculations are done without the phase factors for the excitation fields.[7] The phase convention for the complex absorbance is the same as for the complex cross-section: real parts correspond to absorption; imaginary parts correspond to index-of-refraction. The final state $|f]$ is obtained from the initial, equilibrium state $|eq]$ by successive operators $\mathbf{T}_n$, representing optical transitions due to the nth excitation, and $\mathbf{G}(t_n, t_{n-1})$, representing evolution between times t_{n-1} and t_n,

$$|f(\tau_N, \ldots, \tau_1)]^\circ = \mathbf{G}(t_N, t_{N-1})\mathbf{T}_N^\circ \ldots \mathbf{G}(t_1, t_0)\mathbf{T}_1^\circ |eq]. \tag{4}$$

Throughout the paper, absolute times will be denoted t_n, and time intervals will be given by

$$\tau_n = t_n - t_{n-1}. \tag{5}$$

The equation of motion for an arbitrary state $|P]$ contains the rate operator $\mathbf{R}(t)$

$$\frac{d}{dt}|P] = -\mathbf{R}(t)|P]. \tag{6}$$

For nonexponential relaxations, the rates are time dependent. The Green's operator $\mathbf{G}(t_n, t_{n-1})$ is then nonstationary

$$\mathbf{G}(t_2, t_1) = \exp_+\left(-\int_{t_1}^{t_2} \mathbf{R}(t)dt\right), \tag{7}$$

where the exponential is time ordered.[30]

The optical-transition operator $\mathbf{T}_n^\circ$ is given by

$$\mathbf{T}_n^\circ = \sum_{i,j\in\{a,b\}} I_{n,ij}\, \boldsymbol{\sigma}_T\, \mathbf{K}_{n,ij}(\vec{\mathbf{M}} \cdot \vec{\Pi}_{n,ij}). \tag{8}$$

The nth excitation consists of two pulses labeled a and b (see Fig. 1), and in Eq. (8), the sum runs over the four permutations of these pulses. The effective fluence of the pair $I_{n,ij}$ is the geometric mean of the fluences of the two pulses, $I_{n,i}$ and $I_{n,j}$: $I_{n,ij} = (I_{n,i}I_{n,j})^{1/2}$. The transition cross-section operator $\boldsymbol{\sigma}_T$ is constructed from the absorption cross-sections of the electronic transitions of the system. Unlike the detection cross-section $\boldsymbol{\sigma}_D$, which is complex, $\boldsymbol{\sigma}_T$ has only real elements. The dipole-moment tensor $\vec{\mathbf{M}}$ and the polarization tensor $\vec{\Pi}_{n,ij}$ are required to calculate the effects of chromophore rotation, but will be neglected in this paper. The phase-matching conditions are generated by the grating-vector operator $\mathbf{K}_{n,ij}$. We assume that one combination of pulses is perfectly phase matched, and all others are poorly phase matched.

With these assumptions, the equation for the signal reduces to

$$A^{(N)}(\tau_N, \ldots, \tau_1) = (-1)^N \rho L I^{(N)} [I|\boldsymbol{\sigma}_D \mathbf{G}(t_N, t_{N-1}) \ldots \times \boldsymbol{\sigma}_T \mathbf{G}(t_1, t_0)\boldsymbol{\sigma}_T |eq], \tag{9}$$

with

$$I^{(N)} = I_{N,ab} \cdots I_{1,ab} \tag{10}$$

representing the total excitation fluence from N pulse pairs. In the case where every pulse has the same fluence I, $I^{(N)} = I^N$. The next step is to introduce complete sets of states between each pair of operators in Eq. (9). The results are more compact if we adopt the notation

$$[n|\mathbf{O}|m] = O_n^m \tag{11}$$

for the matrix element of an operator $\mathbf{O}$ between states $[n|$ and $|m]$. Assuming summation over repeated indices, Eq. (9) reduces to

$$\frac{A^{(N)}(\tau_N, \ldots, \tau_1)}{\rho L I^{(N)}} = (-1)^N \left\langle (\sigma_D)_I^n\, G_n^m(t_N, t_{N-1}) \ldots \times (\sigma_T)_k^j\, G_j^i(t_1, t_0)\, (\sigma_T)_i^{eq} \right\rangle. \tag{12}$$

Each term in the implied sum represents one Hilbert-space pathway. This sum is calculated for a single chromophore before averaging over the ensemble, as indicated by the angular brackets.

If the optical cross-sections are independent of time, the time dependence and relative weight of each pathway can be separated

$$\frac{A^{(N)}(\tau_N, \ldots, \tau_1)}{\rho L I^{(N)}} = (-1)^N\, B_{I,\ldots,k,i}^{n,\ldots,j,eq}\; C_{n,\ldots,j}^{m,\ldots,i}(\tau_N, \ldots, \tau_1). \tag{13}$$

Each pathway is defined by the set of intermediate states $\{i, \ldots, n\}$. The dynamics associated with a pathway are given by the correlation-function matrix

$$C_{n,\ldots,j}^{m,\ldots,i}(\tau_N, \ldots, \tau_1) = \left\langle G_n^m(t_N, t_{N-1}) \ldots G_j^i(t_1, t_0) \right\rangle. \tag{14}$$

Each element of this $2N$-dimensional matrix is an N-time-interval correlation function. Each correlation function is the

ensemble average of N time-evolution operators. The relative weight of each pathway is given by

$$B^{n,l,\ldots,eq}_{I,m,\ldots,i} = (\sigma_D)^n_I \ldots (\sigma_T)^j_k \, (\sigma_T)^{eq}_i \, . \tag{15}$$

Because two of its indices are fixed, this matrix also has $2N$ dimensions. Each element gives the total cross-section of the corresponding element of the correlation-function matrix. The scalar product of these two matrices in Eq. (13) sums the correlation functions from all the pathways with their appropriate cross-sections.

B. Basis set to reduce the dimensionality of the problem

Here, we consider the general problem of a good basis set for pathway calculations in a system with $\mathcal{N}$ optical levels, $\{|0], |1], \ldots, |\mathcal{N}-1]\}$. It is desirable to have the initial, equilibrium state $|eq]$ as one member of the basis set. If the state spacing is large, only the lowest state is occupied in equilibrium: $|0] = |eq]$. It is also desirable to have the identity state $[I|$ as a member of the basis set. Thus, in the new, primed basis set, $\{|0'], |1'], \ldots, |\mathcal{N}-1']\}$, we require

$$|0'] = |eq] = |0] \tag{16}$$

and

$$[0'| = [I| = \sum_{n=0}^{\mathcal{N}-1} [n|. \tag{17}$$

With these conditions, all pathways begin with $|0']$ and end with $[0'|$ [see Eqs. (9) and (12)].

An orthogonal basis set cannot satisfy both Eqs. (16) and (17). However, in a nonorthogonal basis, bras and kets need not be identical: they are described by different, dual basis sets.[31] In such a nonorthogonal system, the nonzero kets must be orthogonal to $[0'|$

$$[0'|n'] = [I|n'] = \delta_{0,n}. \tag{18}$$

Because the identity state measures the total population of a state,[5] Eq. (18) means that the nonzero primed kets do not have any net population: they consist only of population differences. As a result, the rate operator $\mathbf{R}(t)$ cannot connect the zero and nonzero kets without changing the total population of the system. These two sets of states, zero prime and nonzero prime, are the irreducible sets resulting from the law of population conservation. In addition, $|0'] = |eq]$ cannot decay; it is unaffected by $\mathbf{R}(t)$. Thus, it is possible to reduce the dimensionality of the rate matrix $R^{i'}_{j'}(t)$ by eliminating its $0'$ row and column.

The exact form of the nonzero states has not been specified. We choose the first excited state $[1'|$ so it is the only nonzero transition out of $|0']$

$$[n'|\boldsymbol{\sigma}_T|0'] = \delta_{n'1'} \, (\sigma_T)^{0'}_{1'} \, . \tag{19}$$

The transition cross-section operator acts on a general state $|P]$ in a perturbative fashion[6]

$$(\mathbf{1} + \lambda\boldsymbol{\sigma}_T)\,|P] = |P] + \lambda\boldsymbol{\sigma}_T|P]. \tag{20}$$

By the conservation of population, $\boldsymbol{\sigma}_T$ acting on any state can only create a new state with no population, that is, a superposition of nonzero primed states. Thus,

$$[0'|\boldsymbol{\sigma}_T|n'] = 0. \tag{21}$$

With Eqs. (19) and (21), the transition cross-section matrix $(\sigma_T)^i_j$ can also be reduced in dimension by eliminating its $0'$ row and column.

This procedure drops one nonzero element $(\sigma_T)^{0'}_{1'}$, which occurs on the first step in every pathway. The effect of this element will be included in a new detection vector $[\sigma_D|$, which is defined by

$$[\sigma_D| = \frac{(\sigma_T)^{0'}_{1'}}{\mathrm{Re}\,(\sigma_D)^{0'}_{0'}} [0'|\boldsymbol{\sigma}_D. \tag{22}$$

Because all pathways end on $[0'|$, the detection matrix and final state can be replaced by this vector. Because there are no transitions into $|0']$, the first element of the detection matrix only occurs in static ($N = 0$) spectroscopy

$$A^{(0)} = \rho L \, (\sigma_D)^{0'}_{0'} \, . \tag{23}$$

For all higher order measurements, the $n = 0$ element of $(\sigma_D)^{n'}$ can be dropped, and the detection vector can be reduced in dimension. The term $\mathrm{Re}\,(\sigma_D)^{0'}_{0'}$ is included in the definition of $[\sigma_D|$ for convenience: Using Eq. (23), the Nth-order absorbance will scale explicitly with the static absorbance $A'^{(0)}$.

Equation (13) can now be re-expressed as

$$\frac{A^{(N)}(\tau_N, \ldots, \tau_1)}{A'^{(0)}} = I^{(N)} \sigma^{n',\ldots,l',j'}_{m',\ldots,k'} \; C^{m',\ldots,k',1'}_{n',\ldots,l',j'}(\tau_N, \ldots, \tau_1), \tag{24}$$

for $N \neq 0$. The total cross-section,

$$\sigma^{n',\ldots,l',j'}_{m',\ldots,k'} = (-1)^N \, (\sigma_D)^{n'} \, (\sigma_T)^{l'}_{m'} \ldots (\sigma_T)^{j'}_{k'} \, , \tag{25}$$

gives the relative weight of each pathway, but is a lower dimensional matrix than $B^{n,\ldots,j,eq}_{I,\ldots,k,i}$ [Eq. (15)]. It contains N cross-sections to match the N fluence factors in $I^{(N)}$. The correlation function is also simplified relative to Eq. (14), because its first index is now fixed. Equation (24) generalizes a familiar expression for the fractional population change in a pump–probe experiment,

$$\frac{\Delta A'(\tau)}{A'_0} = \frac{\Delta\rho(\tau)}{\rho_0} = -I\sigma C(\tau). \tag{26}$$

The indices in Eq. (24) only run over nonzero values. Thus, in the primed basis set, the entire calculation is restricted to nonzero intermediate states, and the problem is reduced by one dimension. The reduction is possible because of the restrictions implied by population conservation.

For a two-level system, Eqs. (16) and (18) completely determine the primed basis set,

$$\begin{aligned} |0'] &= |0], \\ |1'] &= \frac{1}{\sqrt{2}} \left(|1] - |0]\right), \end{aligned} \tag{27}$$

and its dual basis set,

$$\begin{aligned} [0'| &= [1| + [0|, \\ [1'| &= \sqrt{2}[1|. \end{aligned} \tag{28}$$

It is also possible to include population conservation in a two-level system by using an orthogonal basis set.[6] Either approach is viable, but the current one generalizes to multilevel systems.

C. Application to excitonic systems

For more than two states, Eqs. (16) and (18) do not completely define the higher basis states. Choices can be made to further simplify the transition and rate matrices, but more detailed knowledge of the structure of these matrices is needed. We specialize to excitonic systems, which are defined as a set of equally spaced states or groups of nearly degenerate states that undergo optical transitions and relaxation in increments of one "quantum" at a time. The transition and rate matrices of an excitonic system are simplified if the nonzero primed basis kets are chosen to be differences of neighboring states,

$$|n'] = \frac{1}{\sqrt{2}}\left(|n] - |n-1]\right), \quad n \geq 1, \tag{29}$$

with the dual states

$$[n'| = \sqrt{2}\sum_{i=n}^{\mathcal{N}} [i|, \quad n \geq 1. \tag{30}$$

The remainder of the paper focuses on 1D and 2D experiments. These experiments cannot access states higher than |3], so four-level schemes will be sufficient. The standard basis set for such schemes is {|3], |2], |1], |0]} (triexciton, biexciton, exciton, and ground states, respectively). The same rate matrix applies for all schemes,

$$R^{i}_{j}(t) = \begin{pmatrix} k_t(t) & 0 & 0 & 0 \\ -k_t(t) & k_b(t) & 0 & 0 \\ 0 & -k_b(t) & k_e(t) & 0 \\ 0 & 0 & -k_e(t) & 0 \end{pmatrix}, \tag{31}$$

where $k_t(t)$ is the triexciton-to-biexciton rate, $k_b(t)$ is the biexciton-to-exciton rate, and $k_e(t)$ is the exciton-to-ground-state rate. When transformed to the primed basis set, the rate matrix becomes

$$R^{i'}_{j'}(t) = \begin{pmatrix} k_t(t) & 0 & 0 & 0 \\ -k_b(t) & k_b(t) & 0 & 0 \\ 0 & -k_e(t) & k_e(t) & 0 \\ 0 & 0 & 0 & 0 \end{pmatrix}, \tag{32}$$

which can be reduced in dimensionality to

$$R^{i'}_{j'}(t) = \begin{pmatrix} k_t(t) & 0 & 0 \\ -k_b(t) & k_b(t) & 0 \\ 0 & -k_e(t) & k_e(t) \end{pmatrix}. \tag{33}$$

In addition, the total signal given by Eq. (24) simplifies because the first excited state defined by Eq. (19) is also the lowest state in the relaxation scheme given by Eq. (33), that is, $j = 1'$

$$\frac{A^{(N)}(\tau_N, \ldots, \tau_1)}{A'^{(0)}} = I^{(N)}\sigma^{n',\ldots,l',1'}_{m',\ldots,k'}\, C^{m',\ldots,k',1'}_{n',\ldots,l',1'}(\tau_N, \ldots, \tau_1). \tag{34}$$

Thus, the signal is calculated as a product of two $2(N-1)$-dimensional matrices, one dimension lower than in Eq. (13).

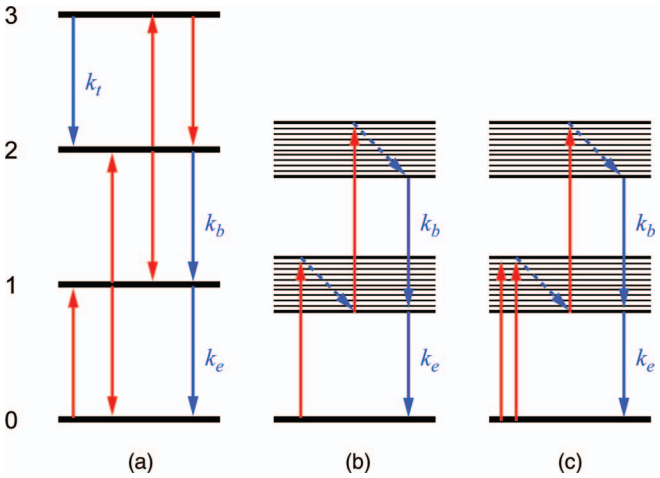

FIG. 2. Three energy-level schemes for an excitonic system. Red arrows are allowed optical transitions with each arrow indicating a factor of σ in cross-section. Blue arrows indicate nonradiative transitions; dashed arrows are fast relaxations.

Off-diagonal elements in the rate matrix add complexity to the calculations. It is not generally possible to diagonalize the rate matrix with any coordinate transformation. However, in the primed basis set, the off-diagonal terms become small if each higher exciton relaxes rapidly compared to lower excitons. As discussed in Sec. IV B below, this limit can be regarded as one of strong incoherent coupling. In the current example,

$$R^{i'}_{j'}(t) \xrightarrow{k_t \gg k_b \gg k_e} \begin{pmatrix} k_t(t) & 0 & 0 \\ 0 & k_b(t) & 0 \\ 0 & 0 & k_e(t) \end{pmatrix}. \tag{35}$$

The transition and detection cross-section matrices depend on the spectroscopic details of the system. Three examples are shown in Fig. 2. They have been chosen to illustrate important limiting behaviors in the final signal. Scheme A represents an exciton consisting of many coupled chromophores ($M \to \infty$, see Sec. IV B). The ground-to-exciton transition has the same cross-section as the exciton-to-biexciton and biexciton-to-triexciton transitions: $\sigma_{01} = \sigma_{12} = \sigma_{23} = \sigma$. In addition, the downward transitions have the same cross-section as the upward transitions: $\sigma_{01} = \sigma_{10}$, $\sigma_{12} = \sigma_{21}$ and $\sigma_{23} = \sigma_{32}$.

Alternatively, the exciton levels may not be eigenstates. They may have internal structure or dynamics within a band of nearly degenerate eigenstates. Scheme B is an example. Absorption to a bright state is followed by rapid relaxation to a state with zero emission cross-section: $\sigma_{10} = \sigma_{21} = 0$. The ground-to-exciton and exciton-to-biexciton transitions still have the same strength: $\sigma_{01} = \sigma_{12} = \sigma$. No triexciton state is included.

Scheme C is similar to Scheme B, in that it has no triexciton and no emission ($\sigma_{10} = \sigma_{21} = 0$). However, it consists of few coupled chromophores, so the exciton-to-biexciton transition has a lower cross-section than the ground-to-exciton transition. We choose $\sigma_{01} = 2\sigma_{12} = 2\sigma$ ($M = 2$, see Sec. IV B). CdSe nanoparticles with band-edge excitation are a real system approximated by model C.[11,12,32]

For Scheme A in the standard basis set, the transition matrix is

$$(\sigma_T)^{i}_{j} = \sigma' \begin{pmatrix} -1 & 1 & 0 & 0 \\ 1 & -2 & 1 & 0 \\ 0 & 1 & -2 & 1 \\ 0 & 0 & 1 & -1 \end{pmatrix}, \tag{36}$$

and the detection matrix is

$$(\sigma_D)^{i}_{j} = \frac{\sigma}{2} \begin{pmatrix} -1 & 1 & 0 & 0 \\ -1 & 0 & 1 & 0 \\ 0 & -1 & 0 & 1 \\ 0 & 0 & -1 & 1 \end{pmatrix}, \tag{37}$$

where the prime indicates the real part of the complex cross-section. In the primed basis set, these matrices become

$$(\sigma_T)^{i'}_{j'} = \sigma' \begin{pmatrix} -2 & 1 & 0 & 0 \\ 1 & -2 & 1 & 0 \\ 0 & 1 & -2 & \sqrt{2} \\ 0 & 0 & 0 & 0 \end{pmatrix} \tag{38}$$

and

$$(\sigma_D)^{i'}_{j'} = \frac{\sigma}{2} \begin{pmatrix} -2 & 1 & 0 & 0 \\ -3 & 0 & 1 & 0 \\ -2 & -1 & 0 & \sqrt{2} \\ -\sqrt{2} & 0 & -\sqrt{2} & 2 \end{pmatrix}. \tag{39}$$

Reducing the dimensionality of the matrices yields

$$(\sigma_T)^{i'}_{j'} = \sigma' \begin{pmatrix} -2 & 1 & 0 \\ 1 & -2 & 1 \\ 0 & 1 & -2 \end{pmatrix} \tag{40}$$

and

$$(\sigma_D)^{i'} = \sigma \begin{pmatrix} -1 & 0 & -1 \end{pmatrix}. \tag{41}$$

To evaluate the total signal for Scheme A, Eqs. (40) and (41) are inserted into Eq. (25) and evaluated by standard matrix methods to yield the relative cross-section of each pathway $\sigma^{n',\ldots,l',1'}_{m',\ldots,k'}$. The correlation function for each pathway $C^{m',\ldots,k',1'}_{n',\ldots,l',1'}(\tau_N, \ldots, \tau_1)$ is evaluated by putting Eq. (33) into Eqs. (7) and (14). These components are put into Eq. (34) to give the experimental signal. Examples of this procedure are given in Sec. III.

III. PATHWAY CALCULATIONS IN EXCITONIC SYSTEMS

A. Cross-sections

In the standard basis set, Eq. (13) yields three pathways with nonzero amplitude for 1D experiments and 16 pathways for 2D experiments. In the primed basis set using Eq. (34), the number of pathways is reduced to one for 1D experiments and three for 2D experiments. These pathways are shown on the right-hand side of Fig. 3. Each pathway is represented as a series of transformation from the initial state on the right to the final state on the left. Each transformation is represented as an arrow and contributes a matrix element of the operator governing the transformation, which is shown below the pathways. The final state of each pathway is detected by forming the product with the detection vector $[\sigma_D|$. The strong

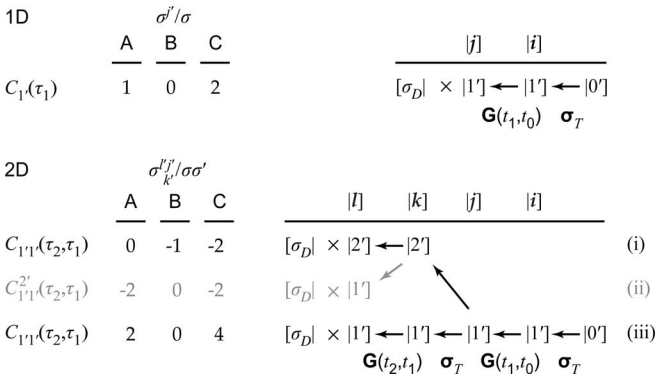

FIG. 3. Pathways for the calculation of one-dimensional (1D) and two-dimensional (2D) signals. The right-hand side shows the allowed pathways between states $|n']$ in the primed basis set. The operators responsible for each transition are given below the arrows: $\mathbf{G}$, the time-evolution operator and $\boldsymbol{\sigma}_{T'}$ the optical transition operator. The indices corresponding to each level in the pathway are indicated above the solid line. The final state in each pathway is detected by taking the product with the detection vector $[\sigma_D|$. The total cross-section for each pathway is given in the center of the figure for each of the energy-level schemes shown in Fig. 2. The correlation function for each pathway is given on the left. Pathways (i) and (iii) have only diagonal relaxation and dominate when the biexciton decay is faster than the exciton decay. Pathway (ii) (gray) involves cross-relaxation and is a minor contribution.

selection rules in the primed basis set allow one to quickly enumerate the pathways with nonzero amplitude on such diagrams.

The correlation function corresponding to each pathway is shown on the left-hand side of Fig. 3. It is formed from the matrix elements of the time-evolution operator of the corresponding pathway through Eq. (14). The steps in the pathways are labeled above the solid line with the indices used in our equations.

In the case where biexciton relaxation is faster than exciton relaxation, pathway (ii), which is in gray, has only a small contribution. That pathway will be discussed in Sec. III C. For now, we only consider the two dominant 2D pathways. Note that the triexciton state contributes to the detection cross-section in Scheme A, but $|3']$ cannot occur as an intermediate state in a 2D experiment.

The total cross-section for each pathway is calculated from the matrix elements of the cross-section operators, $\boldsymbol{\sigma}_T$ and $\boldsymbol{\sigma}_D$, according to Eq. (25). The exact cross-section for each pathway and, in particular, the relative contributions of exciton and biexciton dynamics, depends on the details of the state scheme. Results for the three schemes of Fig. 2 are shown in the center of Fig. 3. Scheme A is a limiting case (see Sec. IV B below) where excitons are detectable and biexcitons are not. The only pathway involving biexciton dynamics, pathway (i), has a cross-section of zero. Scheme B is in the opposite limit: biexcitons are directly detectable and excitons are not. Scheme B gives no signal in a 1D experiment, and 2D pathway (iii) has a cross-section of zero. However, 2D pathway (i) has a nonzero cross-section and can be measured in Scheme B. Information on both exciton and biexciton dynamics are available from this pathway.

Scheme C is an intermediate case where pathways ending with either excitons or biexcitons contribute to the signal. The notable feature is that the two pathways (i) and (iii) have

opposite signs. Generally, the biexciton relaxes faster than the exciton, and the signal will initially rise as the negative biexciton signal decays. This feature allows 2D MUPPETS to cleanly separate exciton and biexciton dynamics, as will be illustrated in Sec. IV A.

To summarize, the relative contributions of exciton and biexciton dynamics to a 2D experiment vary with the transition cross-sections of the system of interest. These cross-sections determine both the relative signs and magnitudes of the correlation functions that are measured, and thus, the type of dynamical information that is available.

B. Diagonal correlation functions

The reduction in the number of pathways in the primed basis set not only simplifies the calculation of the amplitudes; it also reduces the number of correlation functions to a minimum. Figure 3 shows that a 1D experiment is described by a single correlation function $C_{1'}^{1'}(\tau_1)$. This correlation function is diagonal in the sense that in one time period it only measures survival of one basis state. In this case, the notation can be simplified: $C_i^i(\tau_1) = C_i(\tau_1)$. This type of correlation function is normalized to one at the time origin.

Using Eqs. (7), (14) and (33), the exciton decay measured in a 1D experiment is given by

$$C_{1'}(\tau_1) = \left\langle G_{1'}^{1'}(t_1, t_0)\right\rangle = \left\langle \exp\left(-\int_{t_0}^{t_1} k_e(t)dt\right)\right\rangle. \quad (42)$$

A similar correlation function,

$$C_{2'}(\tau_1) = \left\langle G_{2'}^{2'}(t_1, t_0)\right\rangle = \left\langle \exp\left(-\int_{t_0}^{t_1} k_b(t)dt\right)\right\rangle, \quad (43)$$

defines the biexciton decay, but it cannot be measured in a 1D experiment.

The 2D signals are dominated by diagonal correlation functions. The exciton–exciton correlation function,

$$C_{1'1'}(\tau_2, \tau_1) = \left\langle G_{1'}^{1'}(t_2, t_1)G_{1'}^{1'}(t_1, t_0)\right\rangle = \left\langle \exp\left(-\int_{t_1}^{t_2} k_e(t)dt - \int_{t_0}^{t_1} k_e(t)dt\right)\right\rangle, \quad (44)$$

occurs in pathway (iii) of Fig. 3. It is essentially similar to the 2D correlation function previously studied in two-level systems.[3,8,10] If the decay is nonexponential due to homogeneous causes, the 2D correlation function is the product of 1D correlation functions,

$$C_{1'1'}(\tau_2, \tau_1) = C_{1'}(\tau_2)C_{1'}(\tau_1). \quad (45)$$

If the decay is heterogeneous, the 2D correlation function is equal to the 1D correlation function of the sum of the time variables,

$$C_{1'1'}(\tau_2, \tau_1) = C_{1'}(\tau_2 + \tau_1). \quad (46)$$

Thus, with 2D MUPPETS in an excitonic system, it is possible to distinguish homogeneous and heterogeneous mechanisms of rate dispersion of the exciton decay, just as it is in a two-level system.

A new feature of MUPPETS in multilevel systems is the possibility of cross-correlations between different relaxations. For example, pathway (i) in Fig. 3 has an exciton–biexciton correlation function,

$$C_{2'1'}(\tau_2, \tau_1) = \left\langle G_{2'}^{2'}(t_2, t_1)G_{1'}^{1'}(t_1, t_0)\right\rangle = \left\langle \exp\left(-\int_{t_1}^{t_2} k_b(t)dt - \int_{t_0}^{t_1} k_e(t)dt\right)\right\rangle. \quad (47)$$

Although two transitions are involved, the correlation is still diagonal during each time interval. When $\tau_1 = 0$, this function gives access to the biexciton decay [Eq. (43)],

$$C_{2'1'}(\tau_2, 0) = C_{2'}(\tau_2). \quad (48)$$

More generally, $C_{2'1'}(\tau_2, \tau_1)$ is sensitive to correlations between exciton and biexciton dynamics. These correlations are an important new feature in multilevel MUPPETS and are illustrated with examples in Sec. IV C.

C. Off-diagonal correlation functions

In addition to the diagonal correlation functions just discussed, multilevel systems also have correlations involving relaxation between basis states during one of the time periods. These correlation functions involve off-diagonal elements of the rate matrix. For example, pathway (ii) in Fig. 3 has the correlation function

$$C_{1'1'}^{2'}(\tau_2, \tau_1) = \left\langle G_{1'}^{2'}(t_2, t_1)G_{1'}^{1'}(t_1, t_0)\right\rangle, \quad (49)$$

which involves relaxation from $|2'\rangle$ to $|1'\rangle$ during τ_2. The Appendix [see Eq. (A5)] shows that the off-diagonal time evolution can be calculated exactly once a dynamic model for the diagonal elements is specified

$$G_{1'}^{2'}(t_2, t_1) = \int_{t_1}^{t_2} G_{1'}^{1'}(t_2, t')k_{1'}(t')G_{2'}^{2'}(t', t_1)dt'. \quad (50)$$

However, it is difficult to make general statements about the full correlation function from this exact expression.

Fortunately, the primed basis set makes the cross-relaxation small when biexciton relaxation is faster than exciton relaxation. In this case, the relaxation of the standard basis state $|2\rangle$ is biphasic: first $|2\rangle$ decays to $|1\rangle$, and then $|1\rangle$ decays to $|0\rangle$. In the primed basis, this decay is represented by a sum of $G_{2'}^{2'}(t_2, t_1)$ and $G_{1'}^{1'}(t_2, t_1)$. However, this sum contains a small error: the decay of $|1\rangle$ does not start immediately as it does in $G_{1'}^{1'}(t_2, t_1)$; the start of its decay is delayed by the time needed for the biexciton to decay. This correction is isolated as the off-diagonal time evolution $G_{1'}^{2'}(t_2, t_1)$. If the decay of the exciton during the biexciton lifetime is small, the correction is small. The Appendix shows that in this limit, the off-diagonal time evolution can be approximated by [see Eq. (A11)]

$$G_{1'}^{2'}(t_2, t_1) = G_{2'}^{2'}(t_2, t_1)(1 - G_{1'}^{1'}(t_2, t_1)). \quad (51)$$

The cross-relaxation correlation function cannot be calculated until the correlation between exciton and biexciton

dynamics are specified. However, its properties can be illustrated with the case of uncorrelated dynamics. In that case, the 1D and 2D correlation cross-relaxation correlation functions can be expressed in terms of the diagonal correlation functions,

$$C^{2'}_{1'}(\tau_1) = \left\langle G^{2'}_{1'}(t_2, t_1)\right\rangle = C_{2'}(\tau_1)\,(1 - C_{1'}(\tau_1)) \tag{52}$$

and

$$C^{2'}_{1'1'}(\tau_2, \tau_1) = C_{2'}(\tau_2)\,(C_{1'}(\tau_1) - C_{1'1'}(\tau_1, \tau_2))\,. \tag{53}$$

Cross-relaxations are not normalizable: they are zero at the time origin. Their contribution to the signal must be judged not by their cross-section, as given in Fig. 3, but by their maximum size. The 2D function $C^{2'}_{1'1'}(\tau_2, \tau_1)$ is zero whenever $\tau_2 = 0$. Its maximum lies along $\tau_1 = 0$, where it is equal to the 1D cross-relaxation function,

$$C^{2'}_{1'1'}(\tau_2, 0) = C^{2'}_{1'}(\tau_2). \tag{54}$$

It rises slowly in τ_2 with the exciton decay $C_{1'}(\tau_2)$, but is cut off by the rapid biexciton decay $C_{2'}(\tau_2)$ [see Eq. (52) and Fig. 4(a)]. If the dynamics can be characterized by average rate constants, the maximum value of $C^{2'}_{1'}(\tau_2)$ is approximately k_e/k_b.

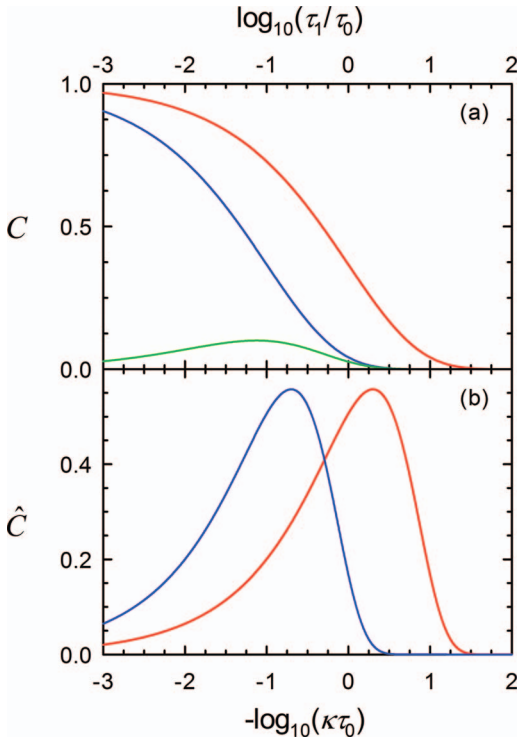

FIG. 4. The 1D kinetics used in the example calculations (Figs. 5–7), which are identical for all the models. (a) Time decays: exciton decay $C_{1'}(\tau)$ [upper, red curve, Eq. (55)], biexciton decay $C_{2'}(\tau)$ [middle, blue curve, Eq. (56)], and cross-relaxation $C^{2'}_{1'}(\tau_1)$ [lowest, green curve, Eq. (52)]. (b) Rate spectra: Exciton spectrum $\hat{C}_{1'}(y)$ (rightmost, red curve) and biexciton spectrum $\hat{C}_{2'}(y)$ (leftmost, blue curve) with $y = \ln(\kappa\tau_0)$.

IV. EXAMPLES OF NEW EFFECTS

A. Separating exciton and biexciton dynamics

This section will present calculations of 2D-MUPPETS results for several simple models of the dynamics. All the models are based on state Scheme C in Fig. 2, where all pathways are active. The 1D correlation functions for all the examples will be the same

$$C_{1'}(\tau_1) = \exp[-(\tau_1/\tau_0)^{1/2}] \tag{55}$$

for the exciton and

$$C_{2'}(\tau_1) = \exp[-(10\tau_1/\tau_0)^{1/2}] \tag{56}$$

for the biexciton. These two decays are similar,

$$C_{2'}(\tau_1) = C_{1'}(c\tau_1), \tag{57}$$

with the biexciton decaying ten times faster ($c = 10$) than the exciton.

The decays are stretched exponentials in time and are shown in Fig. 4(a). The cross-relaxation $C^{2'}_{1'}(\tau_1)$ in the uncorrelated limit [Eq. (52)] is also shown in Fig. 4(a). As expected, the large difference between exciton and biexciton decay times makes this term small.

In addition to the time-domain decays, it is useful to look at rate spectra. The rate spectrum $\hat{C}(y)$ of a correlation function $C(\tau)$ is defined implicitly by

$$C(\tau) = \int_{-\infty}^{\infty} \hat{C}(y)\exp(-\tau e^y/\tau_0)dy. \tag{58}$$

The rate spectrum is essentially the inverse Laplace transform of the time decay expressed on a logarithmic scale, $y = \ln(\kappa\tau_0)$, where κ is the Laplace rate. More detail on the properties and calculation of rate spectra can be found in Ref. 2. The rate spectrum $\hat{C}_{1'}(y)$ of the stretched exponential in Eq. (55) is shown in Fig. 4(b). Applying the transform in Eq. (58) twice, a 2D time function $C(\tau_2, \tau_1)$ can be expressed as a rate-correlation spectrum $\hat{C}(y_2, y_1)$.

The experimental signal in a 1D experiment is directly related to the 1D exciton correlation function,

$$A^{(1)}(\tau_1) = 2\sigma I^{(1)} A'^{(0)} C_{1'}(\tau_1). \tag{59}$$

The other 1D correlation functions cannot be observed in a 1D experiment, but they can be accessed in a 2D experiment. The full 2D signal is

$$A^{(2)}(\tau_2, \tau_1) = 2\sigma\sigma' I^{(2)} A'^{(0)}\big(C_{1'1'}(\tau_2, \tau_1) - \tfrac{1}{2}C_{2'1'}(\tau_2, \tau_1) - \tfrac{1}{2}C^{2'}_{1'1'}(\tau_2, \tau_1)\big). \tag{60}$$

Along the $\tau_2 = 0$ axis, the 2D experiment simply duplicates the information in the 1D experiment

$$A^{(2)}(0, \tau_1) = \sigma\sigma' I^{(2)} A'^{(0)} C_{1'}(\tau_1) = \tfrac{1}{2}\sigma' I_2 A^{(1)}(\tau_1). \tag{61}$$

Along the $\tau_1 = 0$ axis, the 2D absorbance reduces to a sum of the three 1D correlation functions,

$$A^{(2)}(\tau_2, 0) = 2\sigma\sigma' I^{(2)} A'^{(0)}\left(C_{1'}(\tau_2) - \tfrac{1}{2}C_{2'}(\tau_2) - \tfrac{1}{2}C^{1'}_{2'}(\tau_2)\right). \tag{62}$$

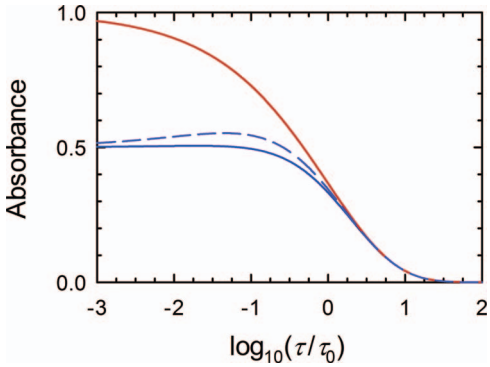

FIG. 5. Two zero-time cuts through the 2D MUPPETS signal. Red (upper) curve: $2A^{(2)}(0, \tau_1)$, which is equivalent to the exciton decay measured in a 1D experiment. Blue (lower) solid curve: $A^{(2)}(\tau_2, 0)$, which has a negative biexciton signal superimposed on the positive exciton signal. The dashed blue curve neglects the cross-relaxation [Eq. (53)]. The curves are normalized to the same amplitude at long time, so the difference between these cuts measures the biexciton decay [Eq. (63)].

These two cuts through the 2D signal are shown in Fig. 5 as solid curves. Because they are related to 1D correlation functions, they contain no new information on rate heterogeneity or correlation. Nonetheless, they contain new information on the biexciton decay that is not available from 1D measurements.

In a two-level system, these two cuts are identical.[2,8,10] Thus, the asymmetry in τ_1 and τ_2 is diagnostic of a biexciton contribution to the signal. Because the two contributions have opposite signs, the cut along $\tau_1 = 0$ may not be monotonic: it can rise as the negative biexciton contribution decays. This feature is also unique to a multilevel system. The effect is weak for the parameters chosen here, but it can be more prominent under other conditions.[11,12] It is more clearly seen in the dashed blue curve in Fig. 5, which leaves out the effects of cross-relaxation.

This feature gives MUPPETS a unique potential to separate exciton and biexciton dynamics. Subtracting the two zero-time cuts [Eqs. (61) and (62)] gives the biexciton decay

$$\frac{2A^{(2)}(0, \tau_1) - A^{(2)}(\tau_2, 0)}{\sigma\sigma' I^{(2)} A'^{(0)}} = C_{2'}(\tau_2) + C_{2'}^{1'}(\tau_2). \qquad (63)$$

The small cross-relaxation term can be approximated with Eq. (52) and removed.

In many systems, the exciton shift is too small to spectrally separate exciton and biexciton dynamics. If there is a significant difference in their decay rates, 1D experiments give a power-dependent change in kinetics that can be identified as the contribution of biexcitons. Unfortunately, a long lived photoproduct with a fast exciton decay has exactly the same properties and can be mistaken for a biexciton.[33] In a 2D MUPPETS experiment, a photoproduct with a fast exciton lifetime contributes to $C_{1'}(\tau)$ and is eliminated in Eq. (63). This experiment distinguishes between species that existed before the pulse sequence (photoproducts) and species created during the pulse sequence (biexcitons). This idea is illustrated in more detail by model III below (Sec. IV C 3). It will also be demonstrated experimentally in future papers.[11,12]

This mechanism fundamentally discriminates between exciton and biexciton signals. If a photoproduct is present and its biexciton decay differs from the biexciton decay of the primary species, the measured $C_{2'}(\tau)$ will contain a mixture of both signals. An extrapolation to zero average power is still needed to eliminate this possibility. The forthcoming papers will also explore the power dependence of the MUPPETS signal in more detail and demonstrate the necessary extrapolation.[11,12]

The sign change between exciton and biexciton signals is dependent on having a net absorption from the exciton state (excited-state absorption minus stimulated emission) that is weaker than the absorption from the ground state. This condition is satisfied in most real excitonic systems.

B. Coherent versus incoherent excitons

Any discussion of excitonic systems faces a potential paradox. Any set of zero-order, two-level chromophores can be grouped to form a multilevel system. To avoid a paradox, all multiexciton effects must disappear in the absence of a suitable interaction between the zero-order chromophores. The number of zero-order chromophores to consider is nontrivial in many systems: How many electron-hole pairs in a semiconductor? How many molecules in a dye aggregate? How many "segments" in a conjugated polymer?

First, one cannot define an excitonic system that is overly large. If M zero-order chromophores with an absorption cross-section σ are included, the ground-to-exciton cross-section is $M\sigma$, the exciton-to-biexciton cross-section is $(M-1)\sigma$, and so on. In the limit as M becomes large, Scheme A (Fig. 2) is reached as a limit. In this scheme, the pathways involving multiple excitons have zero amplitude (Fig. 3). The reason is that absorption saturation is lost as M becomes large. Without nonlinear absorption, there can be no signal in a multidimensional experiment.

Second, one must consider the nature of the interaction between chromophores. In spectral correlation spectroscopy, the interaction must perturb the zero-order spectroscopy of the system, either splitting the transitions or transferring absorption strength between exciton and biexciton transitions. This relatively strong coupling is sufficient, but not necessary, to create multiexciton effects in MUPPETS.

We focus on the more difficult case where the zero-order spectra and cross-sections are not perturbed and an exciton would not be seen in spectral measurements

$$(\sigma_{D/T})_{1'}^{0'}(\omega) = 2(\sigma_{D/T})_{2'}^{1'}(\omega). \qquad (64)$$

This equation requires that both the integrated cross-sections and the cross-section at each frequency are not perturbed, that is, there is no coherent coupling. Even without spectral interactions, there can be an interaction that perturbs the rates, for example, one that causes exciton–exciton annihilation. This interaction constitutes an incoherent coupling. This coupling expresses itself primarily through the cross-relaxation function, which we previously calculated in the limit of strong incoherent coupling, $k_b \gg 2k_e$, Eq. (51). In the limit of no coupling, statistics cause the biexciton rate to be twice the

exciton rate,

$$k_b(t) = 2k_e(t), \tag{65}$$

or the biexciton decay to be the square of the exciton decay,

$$G^{2'}_{2'}(t_1, t_0) = \left(G^{1'}_{1'}(t_1, t_0)\right)^2. \tag{66}$$

Putting this zero rate-coupling limit into Eq. (A8) gives

$$G^{2'}_{1'}(t_2, t_1) = G^{1'}_{1'}(t_2, t_1) - G^{2'}_{2'}(t_2, t_1). \tag{67}$$

The relevant 2D cross-relaxation function [Eq. (47)] is then

$$C^{2'}_{1'1'}(\tau_2, \tau_1) = C_{1'1'}(\tau_2, \tau_1) - C_{2'2'}(\tau_2, \tau_1). \tag{68}$$

In the absence of spectral perturbations, the relative cross-sections for the three 2D pathways are those of Scheme C (Fig. 3). With Eq. (68), the cross-relaxation pathway (ii) partially cancels the exciton–exciton pathway (iii), but completely cancels the exciton–biexciton pathway (i). Thus, all multiexciton effects disappear from MUPPETS unless there is an incoherent coupling that violates Eq. (65). Conversely, any deviation from Eq. (65) creates excitonic effects that are detectable in MUPPETS. However, a coherent coupling that violates Eq. (64) is not required. Thus, a system may need to be treated as an incoherent exciton in MUPPETS, even when it does not need to be treated as a coherent exciton in spectral correlation spectroscopy.

The difference between incoherent and coherent excitons is one of degree, not of kind. Consider the interaction energy coupling the zero-order chromophores. The inverse of this energy gives an interaction time that describes the rate of energy transfer between the chromophores. To have a coherent coupling that is detectable in coherent spectroscopy, the interaction time must be on the order of or shorter than the dephasing time, i.e., there must be coherent energy transfer. If the interaction is weaker, it can still induce incoherent energy hopping that leads to exciton–exciton annihilation. So long as the annihilation time is on the order of or shorter than the population decay time, an incoherent coupling will perturb the rates and will be detected by MUPPETS. If the population decay time is longer than the dephasing time, a system may constitute an incoherent exciton, even when it is too weakly coupled to form a coherent exciton.

C. Measuring exciton–biexciton correlations

The full 2D-MUPPETS signal, $A^{(2)}(\tau_2, \tau_1)$ with both τ_1 and τ_2 varying, depends on correlations in the kinetics. The exciton–exciton correlation $C_{1'1'}(\tau_2, \tau_1)$ reports on whether the dispersion in $C_{1'}(\tau_1)$ is due to a homogeneous [Eq. (45)] or a heterogeneous [Eq. (46)] mechanism. This idea has been thoroughly discussed in two-level systems.[2,3,8–10] The new feature in excitonic systems is the exciton–biexciton function $C_{2'1'}(\tau_2, \tau_1)$, which reports on correlations between two different transitions. To illustrate the behavior of this function, we will calculate the 2D-MUPPETS signal for four limiting models: homogeneous or heterogeneous exciton kinetics combined with either correlated or uncorrelated exciton–biexciton kinetics.

The time-domain representation of the final signal for each model is shown in Fig. 6. As discussed in Sec. IV A, the

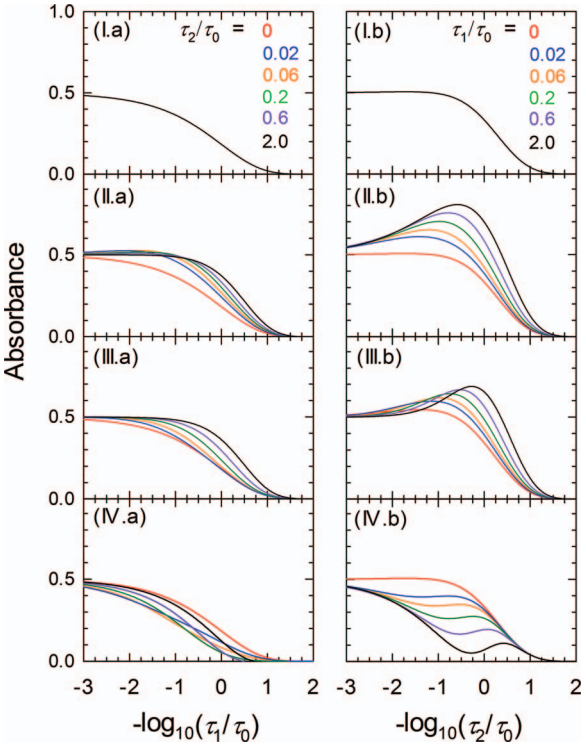

FIG. 6. The total 2D-MUPPETS time decays $A^{(2)}(\tau_2, \tau_1)$ for models I (homogeneous exciton, uncorrelated biexciton), II (heterogeneous exciton, uncorrelated biexciton), III (heterogeneous exciton, correlated biexciton) and IV (homogeneous exciton, correlated biexciton). (a) The signal versus τ_1 for various values of τ_2 normalized at $\tau_1 = 0$. In model I, all curves overlap. (b) The signal versus τ_2 for various values of τ_1 normalized at $\tau_2 = 0$. All models have the same 1D decays (Fig. 4).

decays in τ_1 and in τ_2 are not symmetric, a characteristic of a multilevel system. All the models have identical 1D decays (Fig. 4), but the 2D decays in Fig. 6 are quite different. On an empirical basis, 2D MUPPETS can distinguish different levels of exciton heterogeneity and different levels of exciton–biexciton correlation.

A more rational discussion of the different results is possible using the 2D rate spectra of the total signal and the components contributing to it (Fig. 7). In two-level systems, the diagonal of a 2D rate spectrum is always the square of the 1D rate spectrum and is the same for all models.[2] The spectra also have reflection symmetry about the diagonal. In multilevel systems, these features remain in the exciton–exciton components [Fig. 7(I.a–III.a) but are lost in the total spectra [Fig. 7(I.c–III.c)].

1. Model I: Homogeneous exciton and uncorrelated biexciton

In model I, all the particles are identical, i.e., there is no heterogeneity. The exciton decay of any single chromophore is dispersed due to a complex relaxation mechanism, i.e., the dispersion is homogeneous. In this case, the exciton–exciton correlation function in time is given by Eq. (45). The corresponding rate spectrum,

$$\hat{C}_{1'1'}(y_2, y_1) = \hat{C}_{1'}(y_2)\hat{C}_{1'}(y_1), \tag{69}$$

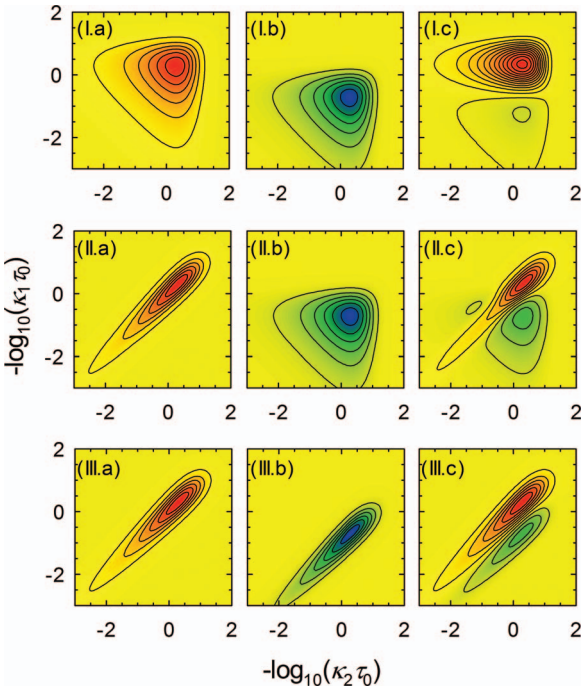

FIG. 7. 2D-MUPPETS rate spectra for models I (homogeneous exciton, uncorrelated biexciton), II (heterogeneous exciton, uncorrelated biexciton) and III (heterogeneous exciton, correlated biexciton). (a) The exciton–exciton component, $\hat{C}_{1'1'}(y_2, y_1)$, with $y = \log_{10}(\kappa\tau_0)$. (b) The negative of the exciton–biexciton component, $-\hat{C}_{2'1'}(y_2, y_1)$. (c) The total signal, $\hat{A}(y_2, y_1) \propto \hat{C}_{1'1'}(y_2, y_1) - \frac{1}{2}\hat{C}_{2'1'}(y_2, y_1) - \frac{1}{2}\hat{C}^{2'}_{1'1'}(y_2, y_1)$. Delta functions have been broadened by a Gaussian with a width of 0.3 decades. Contours are linear with red/orange positive, yellow zero, green/blue negative.

is shown in Fig. 7(I.a). The amplitude along the diagonal is the square of the 1D exciton spectrum in Fig. 4(b).[2] In this model, the off-diagonal amplitude takes on its maximum value everywhere. If the decays were modeled with discrete rates instead of continuous distributions, the off-diagonal amplitude would appear as cross peaks linking rates lying on the diagonal.[2] The off-diagonal amplitude shows that the corresponding diagonal rates are components of a single, complex relaxation process: the diagonal rates "co-exist" on the same chromophore.

Model I additionally assumes that the exciton and biexciton relax by independent and unrelated mechanisms. Thus, the exciton and biexciton kinetics are uncorrelated

$$C_{2'1'}(\tau_2, \tau_1) = C_{2'}(\tau_2)C_{1'}(\tau_1). \tag{70}$$

The negative of the corresponding rate spectrum,

$$\hat{C}_{2'1'}(y_2, y_1) = \hat{C}_{2'}(y_2)\hat{C}_{1'}(y_1), \tag{71}$$

is shown in Fig. 7(I.b). The spectrum is no longer centered on the diagonal, but rather on a shifted, parallel line. The spectrum shows strong amplitude off this line, just as the exciton–exciton spectrum shows strong off-diagonal amplitude. Thus, rate homogeneity of a single transition [Eqs. (45) and (69)] is analogous to a lack of correlation in the rates of two transitions [Eqs. (70) and (71)]. In either case, knowing that a rate is observed on a given chromophore in one measurement does not give any additional information on whether a different rate will be observed on the same chromophore in a second measurement.

The identifying characteristic of fully homogeneous/uncorrelated kinetics is that the 2D signal is separable in the two time variables or in the two rate variables. This separability extends to the cross-relaxation [Eqs. (45) and (53)] and thus, to the total signal. In the time decays of Figs. 6(I.a) and 6(I.b), separability causes all the curves in either plot to overlap after normalization. In the rate spectra, it is this separability that leads to a maximal spread along the anti-diagonal direction.

Figure 7(I.c) shows the rate spectrum of the total signal, including the cross-relaxation. There is strong overlap of the exciton–exciton and exciton–biexciton components, but enough information remains to identify the important features of each component. A horizontal node is formed by cancellation between the exciton–exciton and exciton–biexciton components. The horizontal node reflects the separability of the total signal and, thus, is an identifying feature of a homogeneous and uncorrelated system.

2. Model II: Heterogeneous exciton and uncorrelated biexciton

In model II, each chromophore has a simple, exponential exciton decay, i.e., there is no homogeneous dispersion. The dispersion of the ensemble decay [Eq. (55)] is only due to differences in the decay rates of different chromophores, i.e., the dispersion is due to heterogeneity. In this case, the exciton–exciton correlation function is given by Eq. (46). The corresponding rate-correlation spectrum,

$$\hat{C}_{1'1'}(y_2, y_1) = \hat{C}_{1'}(y_1)\delta(y_1 - y_2), \tag{72}$$

is shown in Fig. 7(II.a). The diagonal amplitude is identical with that of model I [Fig. 7(I.a)]. However in model II, there is no off-diagonal amplitude. The lack of off-diagonal amplitude indicates that different rates do not "co-exist" on a single chromophore: each rate is associated with a different chromophore.

As with model I, model II assumes that the exciton and biexciton decay by independent mechanisms. In particular, the exciton heterogeneity has no effect on the biexciton decay. As a result, Eqs. (70) and (71) still hold for the biexciton–exciton correlation function, and Eq. (53) holds for the cross-relaxation. The biexciton–exciton spectrum [Fig. 7(II.b)] is unchanged from model I [Fig. 7(I.b)]. However, the total spectrum [Fig. 7(II.c)] is quite distinct from that of model I [Fig. 7(I.c)].

The corresponding results in the time domain can be interpreted by regarding one time period as a rate-based filter to select a subensemble whose decay is measured in the other time period. Figure 6(II.b) shows the decay in τ_2, which measures the sum of exciton and biexciton decays. As τ_1 increases, the first time period progressively removes chromophores with a fast exciton decay. The exciton component during τ_2 slows as τ_1 increases. However, the biexciton component is unaffected by filtering based on the exciton decay time. As these two components become separated in time, the signal rise due to biexciton decay becomes visibly distinct from the slower exciton decay.

Figure 6(II.a) shows the decay in τ_1, which measures only the exciton decay. When $\tau_2 = 0$, all chromophores are measured. As τ_2 increases, the second time period progressively selects for chromophores with well-separated exciton and biexciton lifetimes, as these have less signal cancellation. With no correlation between exciton and biexciton lifetimes, these are the chromophores with a long exciton lifetime. Thus, the exciton decay in τ_1 slows as τ_2 increases.

3. Model III: Heterogeneous exciton and correlated biexciton

We now introduce exciton–biexciton correlation. Whereas lack of correlation always produces the same result regardless of the mechanistic details, models with correlation require a more detailed specification of how the correlation is produced. Model III assumes that the exciton and biexciton decays of an individual chromophore are both exponential, that is,

$$G_{1'}^{1'}(t_1, t_0; \theta) = e^{-k_e(\theta)(t_1 - t_0)} \tag{73}$$

and

$$G_{2'}^{2'}(t_1, t_0; \theta) = e^{-k_b(\theta)(t_1 - t_0)}. \tag{74}$$

Dispersion in the ensemble decay is only due to heterogeneity. In Eqs. (73) and (74), the rate is constant in time, but varies with θ, a static or slow bath variable that varies from chromophore to chromophore. This variable has a probability distribution $D(\theta)$, giving the 1D correlation functions

$$C_{1'}(\tau) = \int D(\theta) e^{-k_e(\theta)\tau}\, d\theta \tag{75}$$

and

$$C_{2'}(\tau) = \int D(\theta) e^{-k_b(\theta)\tau}\, d\theta. \tag{76}$$

As in model II, Eqs. (46) and (72) give the heterogeneous exciton–exciton time decay and rate spectrum [Fig. 7(III.a)].

In model I, the exciton and biexciton rates depended on different, independent bath coordinates, $k_e(\theta_e)$ and $k_b(\theta_b)$, and so their dynamics are uncorrelated. In model III, correlation occurs because the exciton and biexciton rates depend on the same bath variable [Eqs. (73) and (74)]. The exact nature of the common dependence must also be specified. For purposes of illustration, we choose

$$k_b(\theta) = c k_e(\theta), \tag{77}$$

which is consistent with the similarity of the exciton and biexciton decay shapes that we have already assumed [Eq. (57)]. The biexciton–exciton correlation function [Eq. (47)],

$$C_{2'1'}(\tau_2, \tau_1) = \int D(\theta) G_{2'}^{2'}(t_2, t_1; \theta) G_{1'}^{1'}(t_1, t_0; \theta)\, d\theta, \tag{78}$$

reduces to

$$C_{2'1'}(\tau_2, \tau_1) = C_{1'}(c\tau_2 + \tau_1) = C_{2'}(\tau_2 + \tau_1/c). \tag{79}$$

When $c = 1$, this equation reduces to the exciton–exciton result for pure heterogeneity [Eq. (46)]. Thus, pure heterogeneity on a single transition is analogous to perfect correlation between two transitions. In a purely heterogeneous sample, one measurement of the exciton rate on a chromophore gives perfect knowledge of the biexciton rate that will be found in a subsequent measurement.

The negative of the corresponding exciton–biexciton rate spectrum,

$$\hat{C}_{2'1'}(y_2, y_1) = \hat{C}_{1'}(y_1)\delta(y_1 - y_2 + \ln c), \tag{80}$$

is shown in Fig. 7(III.b). The spectrum traces out a curve in the $y_2 - y_1$ plane. With the simple correlation defined by Eq. (77), the curve is a straight line. Others forms would generate more complex curves. In general, an experimental result in the form of a one-dimensional curve is diagnostic for correlated heterogeneity, and the form of the curve allows the form of the correlation to be inferred.

The total rate spectrum and time decay are shown in Fig. 7(III.c) and Fig. 6(III.a and III.b), respectively. These include the cross-relaxation,

$$C_{1'1'}^{2'}(\tau_2, \tau_1) = C_{1'}(c\tau_2 + \tau_1) - C_{1'}((c+1)\tau_2 + \tau_1), \tag{81}$$

which is calculated from Eqs. (49) and (51), and its rate spectrum,

$$\hat{C}_{1'1'}^{2'}(y_2, y_1) = \hat{C}_{1'}(y_1)[\delta(y_1 - y_2 + \ln c) - \delta(y_1 - y_2 + \ln(c+1))]. \tag{82}$$

In this figure, the node of the rate spectrum lies parallel to the diagonal, reflecting the simple linear form of Eq. (77). More generally, the node will reflect the shape of the exciton–biexciton correlation function and, thus, the form of the correlation.

The interpretation of the time decays is similar to that for model II. In Fig. 6(III.b), as τ_1 increases, chromophores with fast relaxing excitons are eliminated from the measurement. In this model, the remaining chromophores have both a slower exciton and a slower biexciton decay. Both the rise and fall of the signal are delayed as τ_1 increases. Figure 6(III.a) shows the converse effect. As τ_2 increases, only chromophores with slow decays (either exciton or biexciton) reach the detection phase of the experiment. The exciton decay of the selected chromophores is measured during τ_1 and slows as the selection criterion becomes stricter.

4. Model IV: Homogeneous exciton and correlated biexciton

Model I considered the case of purely homogeneous dispersion in the exciton and biexciton decays. More precisely, each chromophore had a time dependent rate $k_e(t)$ and $k_b(t)$ for the exciton and biexciton, respectively. Underlying this time-dependence is a bath variable $\varphi(t)$ that is relaxing to a new value in the excited state. In model I, the exciton and biexciton rates depend on different, independent bath coordinates, $k_e(\varphi_e(t))$ and $k_b(\varphi_b(t))$, and so their dynamics were uncorrelated. Model IV makes the same basic assumptions,

$$C_{1'}(\tau_1) = G_{1'}^{1'}(t_1, t_0; \varphi) = \exp\left(-\int_{t_0}^{t_1} k_e(\varphi(t))dt\right) \tag{83}$$

and

$$C_{2'}(\tau_1) = G_{2'}^{2'}(t_1, t_0; \varphi) = \exp\left(-\int_{t_0}^{t_1} k_b(\varphi(t))dt\right), \quad (84)$$

but assumes that the exciton and biexciton decays depend on the same bath property, and so are perfectly correlated.

In the absence of heterogeneity, the exciton–exciton correlation function is the same as in model I [Eqs. (45) and (69)]. The biexciton–exciton correlation function is calculated without ensemble averaging, i.e., from

$$C_{2'1'}(\tau_2, \tau_1) = G_{2'}^{2'}(t_2, t_1) G_{1'}^{1'}(t_1, t_0), \quad (85)$$

but more information on the dynamics of $\varphi(t)$ is needed. We make the simple assumption that the dynamics of $\varphi(t)$ are the same in the exciton and biexciton state. In this case,

$$C_{2'1'}(\tau_2, \tau_1) = \frac{G_{2'}^{2'}(t_2, t_0) G_{1'}^{1'}(t_1, t_0)}{G_{2'}^{2'}(t_1, t_0)} = \frac{C_{2'}(\tau_2 + \tau_1) C_{1'}(\tau_1)}{C_{2'}(\tau_1)}. \quad (86)$$

This result can be interpreted by writing it as

$$C_{2'1'}(\tau_2, \tau_1) = (1 + Z(\tau_2, \tau_1))\, C_{2'}(\tau_2) C_{1'}(\tau_1) \quad (87)$$

with

$$Z(\tau_2, \tau_1) = \frac{C_{2'}(\tau_2 + \tau_1)}{C_{2'}(\tau_2) C_{2'}(\tau_1)} - 1. \quad (88)$$

The function $Z(\tau_2, \tau_1)$ measures the rate dispersion of $C_{2'}(\tau)$. When $C_{2'}(\tau)$ is an exponential, $Z(\tau_2, \tau_1) = 0$ everywhere. When $C_{2'}(\tau)$ is not exponential, $Z(\tau_2, \tau_1)$ is still zero along the $\tau_1 = 0$ and $\tau_2 = 0$ edges of its domain, but it is nonzero in the middle: positive if the rate slows with time, and negative if the rate increases with time. Thus, Eq. (87) has the maximum deviation from the uncorrelated result [Eq. (45)] allowed by the dispersion of $C_{2'}(\tau)$. For our model functions, this deviation is a positive one for large values of τ_1 and τ_2. Under certain conditions, this deviation can give a signal that rises with delay in some regions, for example, in Fig. 6(IV.b). Rate spectra for this model are difficult to calculate and are not easy to interpret and so are not presented.

V. THERMAL SIGNALS IN MULTILEVEL SYSTEMS

A. General formalism

Heterodyned experiments are not only sensitive to resonant absorption from the solute; they are also sensitive to index-of-refraction changes in the solvent due to the heat released by nonradiative decay. In 1D, these effects are called thermal gratings.[13–15] (The total thermal response can be separated into a pure thermal and an acoustic component, but that distinction will not be needed here.) In Ref. 7, we showed how to incorporate thermal effects into pathway calculations of multidimensional experiments. Here that treatment is extended to multilevel systems.

The system states must be expanded to include not only the electronic state of the solute P, but also the energy density of the solvent ε, that is, the state must have the form $|P\,\varepsilon]$. The energy density is measured at the same (suppressed) k-vector

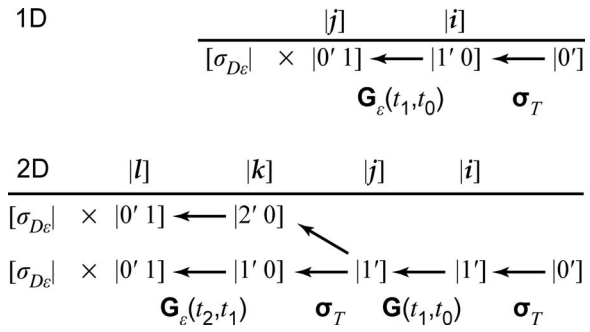

FIG. 8. Pathways for the calculation of thermal signals in one-dimensional (1D) and two-dimensional (2D) experiments [see Fig. 3]. The final two states of the pathways are expanded to $|P\,n_\varepsilon]$ to show both P, the electronic state, and n_ε, the number of quanta of thermal energy deposited in the solvent.

as the electronic state. The response to the solvent energy is linear, so $|P\,\varepsilon_1] + |P\,\varepsilon_2] = |P\,\varepsilon_1 + \varepsilon_2]$. It will be convenient to shift from ε, the heat per volume of solvent, to n_ε, the number of photons of energy converted to heat per solute molecule,

$$n_\varepsilon = \frac{\varepsilon}{\hbar\omega\rho}. \quad (89)$$

An important result of Ref. 7 is that in a multidimensional experiment, only the thermal signal formed by the last excitation is detectable. Thus, the expanded states are only needed at the end of the pathways (see Fig. 8).

The generalized absorption due to thermal effects $A_\varepsilon^{(N)}(\tau_N, \ldots, \tau_1)$ adds to the resonant absorption $A^{(N)}(\tau_N, \ldots, \tau_1)$ [Eq. (9)] and can be expressed in an analogous form,

$$A_\varepsilon^{(N)}(\tau_N, \ldots, \tau_1) = (-1)^N \rho L I^{(N)} [I|\boldsymbol{\sigma}_{D\varepsilon} \times \int_{t_{N-1}}^{t_N} C_\varepsilon(t_N - t') \frac{d}{dt'} \mathbf{G}_\varepsilon(t', t_{N-1})\, dt' \times \ldots \boldsymbol{\sigma}_T \mathbf{G}(t_1, t_0) \boldsymbol{\sigma}_T |eq]. \quad (90)$$

The thermal detection cross-section operator $\boldsymbol{\sigma}_{D\varepsilon}$ can be expressed in terms of $\mathbf{n}_\varepsilon$, the operator that measures the value of n_ε,

$$\boldsymbol{\sigma}_{D\varepsilon} = i\sigma_\varepsilon'' \mathbf{n}_\varepsilon. \quad (91)$$

Because the thermal response is a change in the index-of-refraction, this operator is imaginary. Its magnitude is

$$\sigma_\varepsilon'' = \frac{\omega}{c}\left(1 + \frac{1}{n_s^2}\right)\left(\frac{-dn_s}{d\rho_s}\right)\left(\frac{d\rho_s}{d\varepsilon_s}\right)\hbar\omega, \quad (92)$$

where n_s is the solvent index-of-refraction and ρ_s is the solvent density. This quantity has the units of a cross-section and is normally real and positive. The time-evolution operator for the electronic state $\mathbf{G}(t', t)$ is expanded to $\mathbf{G}_\varepsilon(t', t)$, the time-evolution operator of the combined electronic-thermal state, for the last time period.

The detection is not of the energy itself, but of the resulting change in index-of-refraction. In Eq. (90), the energy deposition is convolved with $C_\varepsilon(\tau)$, the time-evolution of thermal energy into an index-of-refraction change. Sophisticated expressions for $C_\varepsilon(\tau)$ valid over a wide time range are available.[14,34–37] For purposes of illustration over short

times,

$$C_\varepsilon(\tau) = 1 - \cos(2\tau/\Gamma) \tag{93}$$

is an adequate expression.[7] This thermal correlation function is zero when $\tau = 0$ and reaches a maximum of two at half the acoustic period Γ due to interference between the slowly decaying pure thermal response and the more rapidly oscillating acoustic response.

The convolution in Eq. (90) can be removed, if the decay of the electronic state is much faster than the acoustic period. If the decay is not complete within the acoustic period, but only times $\lesssim\Gamma/2$ are treated, this approximation can be pushed farther. The fraction that decays before $\Gamma/4$ (halfway to the maximum) is treated as decaying instantaneously, and the fraction that decays after $\Gamma/4$ is treated as never decaying. This approximation is rough when the solute relaxation has a single timescale, but becomes more reasonable when the decay is highly dispersed in time. In this approximation,

$$\begin{aligned} A_\varepsilon^{(N)}(\tau_N, \ldots, \tau_1) = (-1)^N \rho L I^{(N)} \, [I|\boldsymbol{\sigma}_{D\varepsilon} C_\varepsilon(\tau_N) \\ \times \mathbf{G}_\varepsilon(\Gamma/4 + t_{N-1}, t_{N-1}) \ldots \\ \times \boldsymbol{\sigma}_T \mathbf{G}(t_1, t_0) \boldsymbol{\sigma}_T |eq]. \end{aligned} \tag{94}$$

The primed basis set for electronic states can be introduced for the thermal pathways, as they were for resonant pathways in Sec. II B. The thermal absorption is then written [compare to Eq. (24)]

$$\begin{aligned} \frac{A_\varepsilon^{(N)}(\tau_N, \ldots, \tau_1)}{A'^{(0)}} = I^{(N)} \, (\sigma_\varepsilon)_{m'0,\ldots,k'}^{0'p,\ldots,l',j'} \\ \times (C_\varepsilon)_{0'p,\ldots,l',j'}^{m'0,\ldots,k',1'} (\tau_N, \ldots, \tau_1). \end{aligned} \tag{95}$$

The final two indices are expanded to include the thermal variables. The total thermal cross-section is given by [compare to Eq. (25)]

$$(\sigma_\varepsilon)_{m'0,\ldots,k'}^{n'p,\ldots,l',j'} = (-1)^N \, (\sigma_{D\varepsilon})^{n'p} \, (\sigma_T)_{m'0}^{l'} \ldots (\sigma_T)_{k'}^{j'}. \tag{96}$$

The full operator $\boldsymbol{\sigma}_{D\varepsilon}$ has been reduced by one dimension and converted to a vector as in Eq. (22),

$$[\sigma_{D\varepsilon}| = \frac{(\sigma_T)_{1'}^{0'}}{\mathrm{Re}\,(\sigma_D)_{0'}^{0'}} [0'p|\boldsymbol{\sigma}_{D\varepsilon}, \tag{97}$$

with the result that

$$(\sigma_{D\varepsilon})^{n'p} = i\sqrt{2}\delta_{n'0'}\sigma_\varepsilon'' p. \tag{98}$$

Because $\boldsymbol{\sigma}_{D\varepsilon}$ is diagonal in the electronic state, only the $n' = 0$ elements are nonzero. The multidimensional correlation function in Eq. (95), which corresponds to the one in Eq. (14), is

$$\begin{aligned} (C_\varepsilon)_{0'p,\ldots,j'}^{m'0,\ldots,i'}(\tau_N, \ldots, \tau_1) = C_\varepsilon(\tau_N) \\ \times \left\langle (G_\varepsilon)_{0'p}^{m'0}(\Gamma/4 + t_{N-1}, t_{N-1}) \ldots G_{j'}^{i'}(t_1, t_0) \right\rangle. \end{aligned} \tag{99}$$

The time evolution in the last time period is now governed by the thermal response, rather than by solute dynamics.

B. Results for excitonic systems

In an excitonic system, the number of pathways is severely limited. As with the electronic signal, the primed basis set yields the minimum number of pathways. Figure 8 shows the allowed pathways for $N = 1$ and $N = 2$. Only two elements of $\mathbf{G}_\varepsilon(t', t)$ are needed. In calculating them, we allow nonradiative decay that leads to long lived, high energy states ("trap" states) without the immediate release of heat. The fractional yield of heat for the biexciton-to-exciton and exciton-to-ground transitions are Q_2 and Q_1, respectively. The required matrix elements are then

$$\begin{aligned} (G_\varepsilon)_{0'1}^{1'0}(t', t) = \frac{Q_1}{\sqrt{2}}\left(1 - G_{1'}^{1'}(t', t)\right), \\ (G_\varepsilon)_{0'1}^{2'0}(t', t) = \frac{Q_2}{\sqrt{2}}\left(1 - G_{2'}^{2'}(t', t)\right) + \frac{Q_1}{\sqrt{2}} G_{1'}^{2'}(t', t). \end{aligned} \tag{100}$$

In the primed basis set when the cross-relaxation is small, each thermal pathway is dominated by the relaxation of a single electronic transition.

Combining Eqs. (95)–(100) with the pathways in Fig. 8 yields expressions for the thermal signals,

$$A_\varepsilon^{(1)}(\tau_1) = A'^{(0)} I^{(1)}(-i\sigma_\varepsilon'') C_\varepsilon(\tau_1) Q_1 \, (1 - C_{1'}(\Gamma/4)) \tag{101}$$

and

$$\begin{aligned} A_\varepsilon^{(2)}(\tau_2, \tau_1) = A'^{(0)} I^{(2)}(-i\sigma_\varepsilon'')(2\sigma') C_\varepsilon(\tau_2) \\ \times \left\{ \left(Q_1 - \tfrac{1}{2}Q_2\right) C_{1'}(\tau_1) - Q_1 C_{1'1'}(\Gamma/4, \tau_1) \right. \\ \left. + \tfrac{1}{2}\left[Q_2 C_{2'1'}(\Gamma/4, \tau_1) - Q_1 C_{1'1'}^{2'}(\Gamma/4, \tau_1)\right] \right\}. \end{aligned} \tag{102}$$

The results for the different models in Fig. 2 differ in only minor ways; model C has been used for specificity. The 1D result is consistent with previous work.[13–15] The 2D result is new. It allows the thermal effects to be calculated from the correlation functions already discussed in Sec. IV. The thermal cross-section in the 2D expression can be obtained from 1D experiments. The only new information in the 2D thermal signal is the quantum yield of heat for the biexciton decay. Thus, 2D experiments have the potential to measure this quantity.

VI. CONCLUSIONS

This paper has laid the theoretical foundation for MUPPETS in multilevel systems, especially excitonic systems. The calculations were simplified by introducing a nonorthogonal basis set. By using population conservation, the number of states to be considered was reduced by one. In an excitonic system, the number of pathways and correlation functions are reduced further. An unavoidable complication of multilevel systems is cross-relaxation between basis states. However, suitable approximations were found in the limits of either strong or weak exciton–exciton interaction. Methods for calculating thermal effects in multilevel systems were also presented.

Using these methods, the new information available from MUPPETS was demonstrated. MUPPETS was shown to

be very sensitive to chromophore interactions. First, it was shown that much weaker interactions are needed to observe kinetic effects, that is, to form an incoherent exciton, than are needed to observe spectral effects, that is, to form a coherent exciton. In an incoherent exciton, chromophores interact by incoherent energy hopping followed by exciton–exciton annihilation. Second, it was shown that MUPPETS is a sensitive method for detecting incoherent exciton formation. Any asymmetry in the decays along the two time axes is a sign of an incoherent exciton. The difference between these decays is a direct route to the biexciton decay rate and, thus, to the strength of exciton–exciton interactions. Exciton–exciton annihilation can also be measured by power-dependent 1D experiments, but these measurements can be confounded by the build-up of long-lived photoproducts with short exciton lifetimes. MUPPETS is immune to this problem.

Away from the time axes, MUPPETS offers additional information for systems with rate dispersion. Both exciton rate heterogeneity and correlations between exciton and biexciton dynamics are available. Example calculations suggest that there is sufficient information to allow a unique separation of these two effects in most cases. Rate heterogeneity is a concept that has been explored in previous MUPPETS studies of two-level system; the concept of correlated rates between two transitions is a new one. When the rates of two transitions are correlated, the MUPPETS results are similar to those for heterogeneous rates on a single transition. Correlation indicates that the relaxation mechanisms of the two transitions are linked. Correlation is possible whether the individual relaxations are heterogeneous or homogeneous. In the heterogeneous case, individual particles relax either faster or slower than average for both transitions. In the homogeneous case, the relaxations of both transitions depend on the relaxation of a common bath mode.

The practicality of these ideas will be demonstrated in future papers.[11,12] The results in this paper provide a basis for both a qualitative and quantitative interpretation of those results.

ACKNOWLEDGMENTS

This material is based upon work supported by the National Science Foundation (NSF) under CHE-1111530.

APPENDIX: OFF-DIAGONAL TIME EVOLUTION

The calculation of the off-diagonal elements of the Green's function starts by dividing the time evolution between two times, t_1 and t_2, by M intermediate times t'_a

$$\mathbf{G}(t_2,t_1)=\mathbf{G}(t_2,t'_M)\ldots\mathbf{G}(t'_{a+1},t'_a)\ldots\mathbf{G}(t'_1,t_1). \tag{A1}$$

Taking matrix elements gives

$$G^{2'}_{1'}(t_2,t_1)=G^{n'}_{1'}(t_2,t'_M)\ldots G^{k'}_{l'}(t'_{a+1},t'_a)\ldots G^{2'}_{i'}(t'_1,t_0), \tag{A2}$$

where the indices $i,\ldots,n$ run over all nonzero states. Because relaxation is only downward, all but one of these matrix elements must be diagonal. The only remaining terms are

$$G^{2'}_{1'}(t_2,t_1)=\sum_{a=1}^{N-1}G^{1'}_{1'}(t_2,t'_{a+1})G^{2'}_{1'}(t'_{a+1},t'_a)G^{2'}_{2'}(t'_a,t_1), \tag{A3}$$

where sequences of diagonal elements have been recombined. The limit $M\to\infty$ and $dt'=t'_{a+1}-t'_a\to 0$ can now be applied. Equation (7) provides the infinitesimal Green's operator

$$\mathbf{G}(t+dt',t)=1-\mathbf{R}(t)dt', \tag{A4}$$

resulting in

$$G^{2'}_{1'}(t_2,t_1)=-\int_{t_1}^{t_2}G^{1'}_{1'}(t_2,t')R^{2'}_{1'}(t')G^{2'}_{2'}(t',t_1)dt'. \tag{A5}$$

Using Eq. (32) for the rate matrix element gives Eq. (50) of the main text.

We now use the specific structure of an excitonic rate matrix [Eq. (32)] to replace the off-diagonal rate with a diagonal element

$$G^{2'}_{1'}(t_2,t_1)=\int_{t_1}^{t_2}G^{1'}_{1'}(t_2,t')R^{1'}_{1'}(t')G^{2'}_{2'}(t',t_1)dt'. \tag{A6}$$

Because relaxation is only downward, Eq. (7) also applies to diagonal matrix elements and yields

$$G^{2'}_{1'}(t_2,t_1)=\int_{t_1}^{t_2}\left(\frac{d}{dt'}G^{1'}_{1'}(t_2,t')\right)G^{2'}_{2'}(t',t_1)dt'. \tag{A7}$$

Integration by parts gives

$$G^{2'}_{1'}(t_2,t_1)=G^{2'}_{2'}(t_2,t_1)-G^{1'}_{1'}(t_2,t_1)-\int_{t_1}^{t_2}G^{1'}_{1'}(t_2,t')\left(\frac{d}{dt'}G^{2'}_{2'}(t',t_1)\right)dt'. \tag{A8}$$

This form can be used directly to derive Eq. (67) in the limit of zero incoherent coupling [Eq. (66)].

To look at the opposite limit of strong coupling, we define a change in occupation of $|1'\rangle$,

$$\delta G^{1'}_{1'}(t,t_1)=1-G^{1'}_{1'}(t,t_1), \tag{A9}$$

which is assumed to be small over the biexciton lifetime. The term in Eq. (A8) can be written

$$G^{1'}_{1'}(t_2,t)=\frac{G^{1'}_{1'}(t_2,t_1)}{1-\delta G^{1'}_{1'}(t,t_1)}. \tag{A10}$$

Putting a power series expansion of Eq. (A10) into Eq. (A8) and integrating the first term leads to

$$G^{2'}_{1'}(t_2,t_1)=G^{2'}_{2'}(t_2,t_1)-G^{1'}_{1'}(t_2,t_1)\Big[G^{2'}_{2'}(t_2,t_1)+\int_{t_1}^{t_2}\delta G^{1'}_{1'}(t',t_1)k_2(t')dt'+\frac{1}{2}\int_{t_1}^{t_2}\left(\delta G^{1'}_{1'}(t',t_1)\right)^2k_2(t')dt'+\ldots\Big]. \tag{A11}$$

Keeping only the leading term gives Eq. (51) of the main text. The same results hold if the states $2'$ and $1'$ are replaced by any two neighboring states.

We note that a simple, empirical formula interpolates between the limits of strong [Eq. (51)] and zero [Eq. (67)] incoherent coupling

$$G_{1'}^{2'}(t_2,t_1) = \frac{G_{2'}^{2'}(t_2,t_1)}{G_{1'}^{1'}(t_2,t_1)}\left(1 - G_{1'}^{1'}(t_2,t_1)\right). \tag{A12}$$

The accuracy of this approximation has not been tested.

One can consider couplings outside this range. In this case, the biexciton decay rate is less than twice the exciton decay rate. The presence of a second excitation slows the decay of the first. Although this situation is not forbidden, it is uncommon.

[1]E. van Veldhoven, C. Khurmi, X. Zhang, and M. A. Berg, ChemPhysChem **8**, 1761 (2007).
[2]C. Khurmi and M. A. Berg, J. Chem. Phys. **129**, 064504 (2008).
[3]C. Khurmi and M. A. Berg, J. Phys. Chem. A **112**, 3364 (2008).
[4]C. Khurmi and M. A. Berg, J. Opt. Soc. Am. B **26**, 2357 (2009).
[5]M. A. Berg, J. Chem. Phys. **132**, 144105 (2010).
[6]M. A. Berg, J. Chem. Phys. **132**, 144106 (2010).
[7]K. Sahu and M. A. Berg, J. Chem. Phys. **134**, 144502 (2011).
[8]K. Sahu, S. J. Kern, and M. A. Berg, J. Phys. Chem. A **115**, 7984 (2011).
[9]S. J. Kern, K. Sahu, and M. A. Berg, Nano Lett. **11**, 3493 (2011).
[10]M. A. Berg, Adv. Chem. Phys. **150**, 1 (2012).
[11]K. Sahu, H. Wu, and M. A. Berg, "Rate dispersion in the biexciton decay of CdSe/ZnS nanoparticles from multiple-population period transient spectroscopy," J. Am. Chem. Soc. (to be published).
[12]K. Sahu, H. Wu, and M. A. Berg, "Exciton and biexciton dynamics in CdSe/ZnS nanoparticles by multiple population-period transient spectroscopy (MUPPETS)" (unpublished).
[13]A. von Jena and H. E. Lessing, Opt. Quantum Electron. **11**, 419 (1979).
[14]M. D. Fayer, Annu. Rev. Phys. Chem. **33**, 63 (1982).
[15]H. J. Eichler, *Laser-Induced Dynamic Gratings* (Springer, Berlin, 1986).
[16]E. L. Hahn, Phys. Rev. **80**, 580 (1950).
[17]N. A. Kurnit, I. D. Abella, and S. R. Hartmann, Phys. Rev. Lett. **13**, 567 (1964).
[18]R. R. Ernst, G. Bodenhausen, and A. Wokaun, *Principles of Nuclear Magnetic Resonance in One and Two Dimensions* (Clarendon, Oxford, 1987).
[19]A. Bax, *Two-Dimensional Nuclear Magnetic Resonance in Liquids* (Delft University Press, Delft, Holland, 1982).
[20]D. M. Jonas, Annu. Rev. Phys. Chem. **54**, 425 (2003).
[21]J. Zheng, K. Kwak, and M. D. Fayer, Acc. Chem. Res. **40**, 75 (2007).
[22]A. Remorino and R. M. Hochstrasser, Acc. Chem. Res. **45**, 1896 (2012).
[23]T. Brixner, J. Stenger, H. M. Vaswani, M. Cho, R. E. Blankenship, and G. R. Fleming, Nature (London) **434**, 625 (2005).
[24]N. S. Ginsberg, Y.-C. Cheng, and G. R. Fleming, Acc. Chem. Res. **42**, 1352 (2009).
[25]J. Kim, S. Mukamel, and G. D. Scholes, Acc. Chem. Res. **42**, 1375 (2009).
[26]D. B. Turner, P. Wen, D. H. Arias, and K. A. Nelson, Phys. Rev. B **84**, 165321 (2011).
[27]L. Wang, C. T. Middleton, S. Singh, A. S. Reddy, A. M. Woys, D. B. Strasfeld, P. Marek, D. P. Raleigh, J. J. de Pablo, M. T. Zanni, and J. L. Skinner, J. Am. Chem. Soc. **133**, 16062 (2011).
[28]G. A. Lott, A. Perdomo-Ortiz, J. K. Utterback, J. R. Widom, A. Aspuru-Guzik, and A. H. Marcus, Proc. Natl. Acad. Sci. U.S.A. **108**, 16521 (2011).
[29]J. R. Caram, N. H. C. Lewis, A. F. Fidler, and G. S. Engel, J. Chem. Phys. **136**, 104505 (2012).
[30]S. Mukamel, *Principles of Nonlinear Optical Spectroscopy* (Oxford University Press, New York, 1995).
[31]L. P. Lebedev and M. J. Cloud, *Tensor Analysis* (World Scientific, Singapore, 2003).
[32]V. I. Klimov, Annu. Rev. Phys. Chem. **58**, 635 (2007).
[33]J. A. McGuire, J. Joo, J. M. Pietryga, R. D. Schaller, and V. I. Klimov, Acc. Chem. Res. **41**, 1810 (2008).
[34]L. Genberg, Q. Bao, S. Gracewski, and R. J. D. Miller, Chem. Phys. **131**, 81 (1989).
[35]Y.-X. Yan and K. A. Nelson, J. Chem. Phys. **87**, 6240 (1987).
[36]A. R. Duggal and K. A. Nelson, J. Chem. Phys. **94**, 7677 (1991).
[37]Y. Kimura, M. Fukuda, O. Kajimoto, and M. Terazima, J. Chem. Phys. **125**, 194516 (2006).